Full Paper
doi.org/10.1002/chem.202004633

Chemistry Europe
European Chemical Societies Publishing

Coordination Chemistry

Structurally Modelling the 2-His-1-Carboxylate Facial Triad with a Bulky *N,N,O* Phenolate Ligand

Emily C. Monkcom,[a] Daniël de Bruin,[a] Annemiek J. de Vries,[a] Martin Lutz,[b] Shengfa Ye,[c, d] and Robertus J. M. Klein Gebbink*[a]

Abstract: We present the synthesis and coordination chemistry of a bulky, tripodal *N,N,O* ligand, $\mathbf{Im^{Ph2}NNO^{tBu}}$ (**L**), designed to model the 2-His-1-carboxylate facial triad (2H1C) by means of two imidazole groups and an anionic 2,4-di-*tert*-butyl-subtituted phenolate. Reacting **K-L** with MCl_2 (M = Fe, Zn) affords the isostructural, tetrahedral non-heme complexes [Fe(L)(Cl)] (**1**) and [Zn(L)(Cl)] (**2**) in high yield. The tridentate *N,N,O* ligand coordination observed in their X-ray crystal structures remains intact and well-defined in MeCN and CH_2Cl_2 solution. Reacting **2** with NaSPh affords a tetrahedral zinc thiolate complex, [Zn(L)(SPh)] (**4**), that is relevant to isopenicillin N synthase (IPNS) biomimicry. Cyclic voltammetry studies demonstrate the ligand's redox non-innocence, where phenolate oxidation is the first electrochemical response observed in **K-L**, **2** and **4**. However, the first electrochemical oxidation in **1** is iron-centred, the assignment of which is supported by DFT calculations. Overall, $\mathbf{Im^{Ph2}NNO^{tBu}}$ provides access to well-defined mononuclear, monoligated, *N,N,O*-bound metal complexes, enabling more accurate structural modelling of the 2H1C to be achieved.

Introduction

The 2-His-1-carboxylate facial triad (2H1C) is a bioinorganic motif characterised by the facial, tripodal *N,N,O* coordination of two neutral histidine (His) residues and an anionic carboxylate group, (Asp or Glu), to a single metal centre.[1–3] It occurs at the active site of many oxygen-activating mononuclear non-heme iron enzymes, and is considered one of the most versatile platforms with which nature performs oxidation catalysis.[4,5] The ability of this motif to activate O_2 and mediate a diverse set of highly selective biocatalytic oxidation reactions has attracted the interest of the bioinorganic and catalytic research communities. Many of these reactions are synthetically challenging, and developing small molecular iron-based catalysts that can achieve similar reactivity and selectivity remains a long-standing goal in homogeneous catalysis.

More recently, the 3-His facial triad (3His) has emerged as a recurring bioinorganic motif at the active site of, amongst others, a small group of mononuclear non-heme iron enzymes collectively known as thiol dioxygenases (TDO), which activate O_2 and catalyse the dioxygenation of thiols to their corresponding sulfinic acids.[6] Similarly to the 2H1C, the 3His involves the facial coordination of three amino acid residues to a single iron centre. However, unlike the 2H1C, the 3His comprises three neutral histidine residues, and no carboxylate ligand is required for catalytic activity. In this regard, the different reactivities of isopenicillin N synthase (IPNS), a 2H1C-containing oxidase enzyme, and cysteine dioxygenase (CDO), a TDO enzyme, make for a particularly interesting comparison. In both cases, the native substrate's anionic thiolate binds directly to the iron centre *trans* to a His residue. Yet, in IPNS, O_2 subsequently binds *trans* to an Asp and the δ-(L-α-aminoadipoyl)-L-cysteine-D-valine (ACV) substrate undergoes a 4-electron oxidative bicyclisation,[7–9] whereas in CDO, O_2 binds *trans* to a His residue and the cysteine substrate undergoes sulfur oxygenation (Figure 1).[6,10] This has stimulated a deeper examination of the carboxylate's mechanistic role in 2H1C-containing enzymes. An important strategy to this end is the study of synthetic complexes that model metalloenzyme active sites.

The 2H1C has been an inspiration for the design of many biomimetic ligands,[13] some of the most well-known being the **Tp**,[14] **TPA**,[15] **14-TMC**,[16] **PyTACN**,[17] $\mathbf{PyNMe_3}$,[18] **BPBP**,[19] and **N4Py**[20] ligands (Figure 2, top). These polydentate N-donor ligands support the formation of high-valent iron-oxo species

[a] E. C. Monkcom, D. de Bruin, A. J. de Vries, Prof. Dr. R. J. M. Klein Gebbink
Organic Chemistry and Catalysis, Debye Institute for Nanomaterials Science
Utrecht University, Universiteitsweg 99, 3584 CG Utrecht (The Netherlands)
E-mail: r.j.m.kleingebbink@uu.nl

[b] Dr. M. Lutz
Crystal and Structural Chemistry, Bijvoet Centre for Biomolecular Research
Utrecht University, Padualaan 8, 3584 CH Utrecht (The Netherlands)

[c] Dr. S. Ye
State Key Laboratory of Catalysis, Dalian Institute of Chemical Physics
Chinese Academy of Sciences, 457 Zhongshan Road
Dalian 116023 (P. R. China)

[d] Dr. S. Ye
Max-Planck-Institut für Kohlenforschung
Kaiser-Wilhelm-Platz 1, 45470 Mülheim an der Ruhr (Germany)

Supporting information and the ORCID identification number(s) for the author(s) of this article can be found under:
https://doi.org/10.1002/chem.202004633.

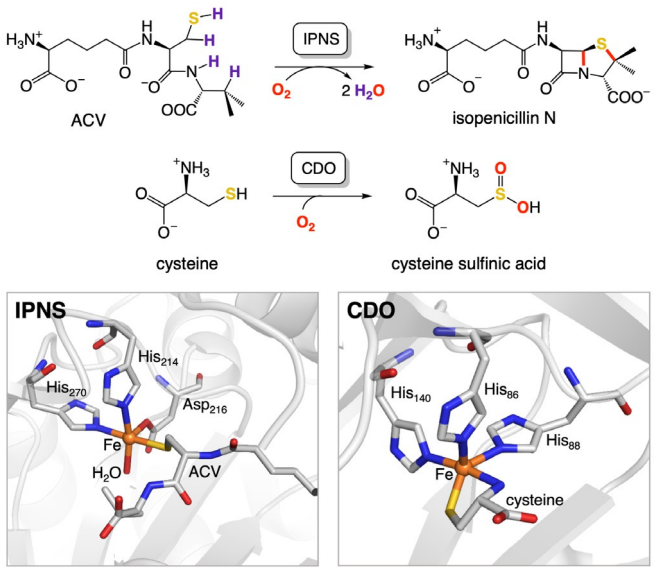

Figure 1. Top: native reactions catalysed by IPNS and CDO. Bottom: the substrate-bound active site structures of IPNS from *Aspergillus nidulans* (PDB 1BK0)[7] and CDO from *Homo sapiens* (PDB 2IC1).[6] Carbon, iron, nitrogen, and oxygen are depicted in grey, orange, blue and red, respectively.

and have greatly helped the scientific community understand the role of such entities in enzymatic reactions and oxidation catalysis.[21,22] However, these ligands can, arguably, be considered structurally more similar to the 3His than the 2H1C due to lack of an anionic O-donor. Moreover, many of these ligands have a denticity greater than three, deviating somewhat from the tricoordinate nature of the 2H1C.

In order to structurally model the 2H1C with greater accuracy, it remains of interest to develop facial, tridentate *N,N,O* ligands. While numerous examples of such ligands with systematically varied donor group constituents have been reported,[23] the number of *N,N,O* ligands that can coordinate in a tripodal manner and support the formation of mononuclear, monoligated metal complexes is small. Typically, difficulties in achieving the desired coordination mode are encountered due to the formation of homoleptic bis-ligand complexes,[24–26] the increase in nuclearity due to anionic O-donor bridging modes,[27–30] or rupture of the *N,N,O* coordination due to lability of a neutral N-/O-donor.[31] The primary strategy to overcome these issues has been to increase the ligand's bite angle and steric demand,[26,31,32] or to use an organic co-ligand.[25,33] In the few cases where monoligation *and* tripodal *N,N,O* coordination were successfully achieved (Figure 2, bottom),[25,26,31–36] little or no further exploration of the solution state behaviour was conducted. The robustness of the ligands' facial *N,N,O* coordination to iron in solution therefore remains largely unknown, making the use of their respective complexes disadvantageous from a practical point of view compared to the well-established coordination chemistry of polydentate N-donor ligands. Previously, our group has explored the facial capping potential of bis-imidazole derived *N,N,O* phenolate ligands, **ImNNO** and **BenzImNNO**.[23,25] However, these were shown to readily form bis-ligated complexes in the absence of a co-ligand. Here, we describe the synthesis of a new *N,N,O* ligand, **Im^{Ph2}NNO^{tBu}** (Figure 3), whose constituent groups have been functionalised with sterically demanding substituents to promote the thermodynamic formation of monoligated, mononuclear metal complexes. While the ligand's imidazole groups are the most biologically relevant heterocycle for modelling histidine residues, the incorporation of a phenol deviates somewhat from the carboxylate residue of the 2H1C due to its redox-active properties. However, the ease with which phenols can be functionalised opens up more possibilities for ligand design and helps avoid certain drawbacks associated to carboxylic acids, such as

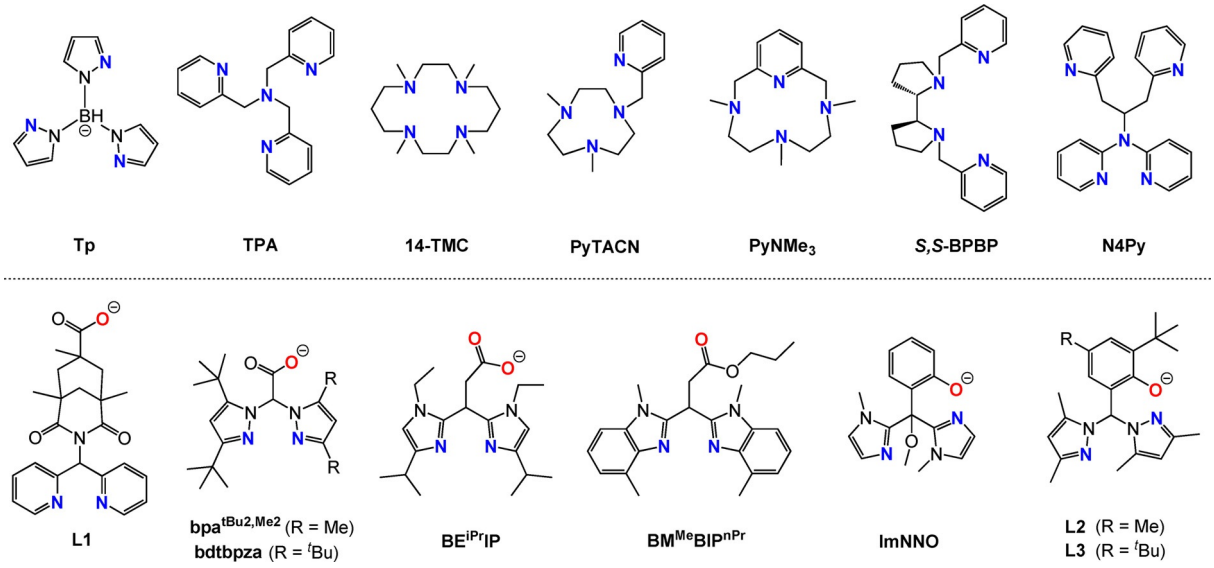

Figure 2. Selected N-donor ligands (top)[11] and tripodal *N,N,O* ligands (bottom)[12] that have been used to synthesise mononuclear, monoligated biomimetic metal complexes. Mononuclear, monoligated iron complexes of **BE^{iPr}IP** and **ImNNO** have only been reported in combination with an organic co-ligand, for example, a catecholate. No mononuclear, monoligated iron complexes have been crystallographically characterised with ligands **bpa^{tBu2,Me2}**, **bdtbpza**, **L2** and **L3**.

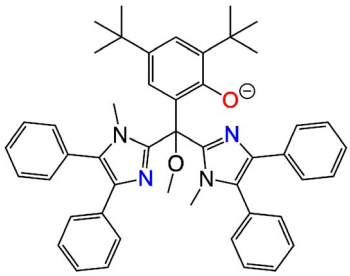

Figure 3. Ligand $\mathbf{Im^{Ph2}NNO^{tBu}}$ with an *N,N,O* donor set.

decarboxylation, poor solubility,[31] or the formation of coordination oligomers.[23] Moreover, the *tert*-butyl substituents on the 2,4-positions of the phenol can help prevent radical side reactions. The coordination chemistry of $\mathbf{Im^{Ph2}NNO^{tBu}}$ is explored with iron and zinc, the latter serving as a convenient diamagnetic analogue with which to conduct detailed studies of the complexes in their solution state. Finally, the synthesis and solution state behaviour of a zinc thiolate complex relevant to IPNS biomimicry is described. In this way, the robustness of the ligand's *N,N,O* facial triad in the presence of biorelevant co-ligands is established, making $\mathbf{Im^{Ph2}NNO^{tBu}}$ an ideal platform with which to model and further investigate the 2H1C.

Results and Discussion

Ligand synthesis and characterisation

Ligand $\mathbf{H\text{-}Im^{Ph2}NNO^{tBu}}$ can be readily synthesised in five steps using a procedure adapted from Jameson et al. (Scheme 1).[25,37] An additional alkylation step has been incorporated to install *tert*-butyl substituents on the phenolate ring.[38] The synthesis also involves the use of 1-methyl-4,5-diphenylimidazole instead of the sterically less encumbered 1-methylimidazole, as our group has previously demonstrated that a higher degree of substitution on the imidazole favours the formation of monoligated complexes.[31] Overall, the synthesis involves the use of readily available starting materials, and the ligand can easily be prepared on a multigram scale. The synthesis begins with the electrophilic aromatic substitution reaction of methyl salicylate with *tert*-butanol in methanol, using sulfuric acid as a catalyst. This results in the formation of **LS1**, which can be recrystallised from methanol and isolated as a white crystalline solid in 51% yield. Next, the salicylate's phenol group is protected using a methyl methoxy ether (MOM), producing **LS2** as a viscous yellow oil in 90% yield. Deprotonation of 1-methyl-4,5-diphenyl-1*H*-imidazole using *n*BuLi, generates a lithium imidazolium salt, two equivalents of which can subsequently perform a nucleophilic attack on the carbonyl group of **LS2**. In doing so, the carbonyl group is reduced to a tertiary alcohol in **LS3**, which is formed in a yield of 89%. Due to its sterically encumbered nature, the subsequent methylation of the tertiary alcohol is kinetically slow and requires a twofold excess of NaH and MeI as well as overnight stirring in order to form compound **LS4** in 82% yield. The final step involves the deprotection of the phenol in acidic conditions to yield the ligand $\mathbf{H\text{-}Im^{Ph2}NNO^{tBu}}$ as an off-white solid in 71% yield. The overall isolated yield of the ligand synthesis is 24%.

The phenol can easily be deprotonated using KH as a base. Stirring the ligand with an excess of KH in THF resulted in the fast release of hydrogen gas as well as a bright yellow solution, indicative of phenol deprotonation. The reaction was left to stir two hours, after which it was filtered to remove any unreacted KH. The solvent was removed under vacuum, affording an off-white crude solid. The solid was washed with hexane and dried, producing the desired potassium ligand salt ($\mathbf{K\text{-}Im^{Ph2}NNO^{tBu}}$) in 92% yield. ^{1}H NMR analysis of the ligand salt in [D_3]acetonitrile (Figure S19) clearly demonstrates the anionic nature of the phenolate through the absence of any OH signal. This is further corroborated by the absence of an O–H stretch in the IR analysis (Figure S21). However, the singlet assigned to the *N*-methyl groups at 3.29 ppm is severely broadened, indicating fluxional exchange of the two imidazole groups at 25 °C. Cooling the measurement to −30 °C produces a spec-

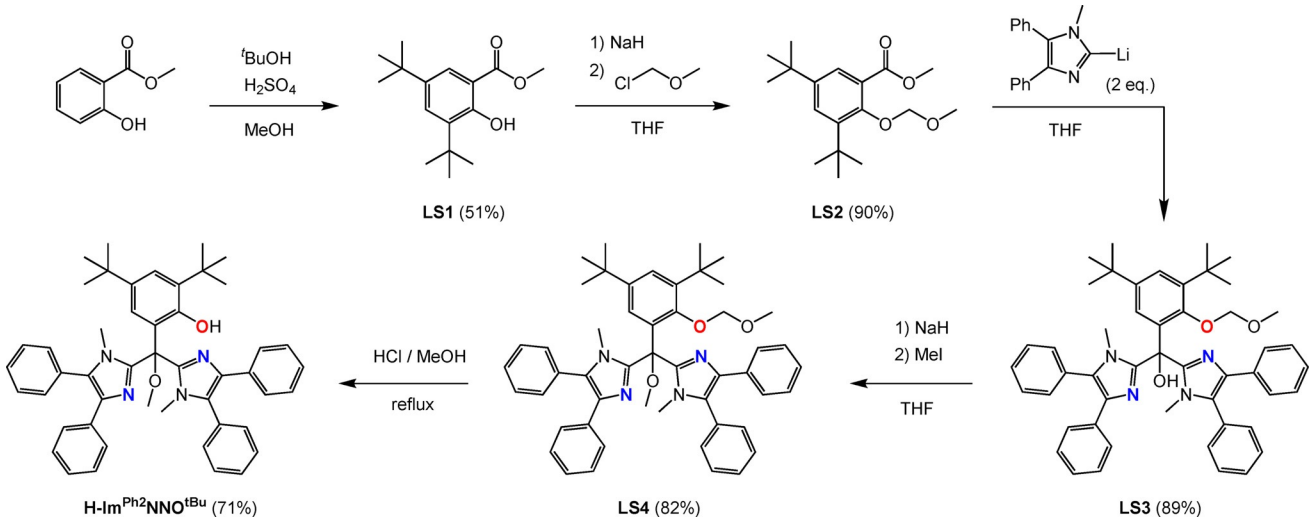

Scheme 1. Synthesis of $\mathbf{H\text{-}Im^{Ph2}NNO^{tBu}}$.

trum with two distinct singlets of equal integration at 3.49 and 2.92 ppm, assigned to the *N*-methyl groups (Figure S20). This suggests that a temperature-dependent fluxional process occurs, possibly involving the dissociation of the imidazole groups from the potassium ion. Crystals of **K-Im^{Ph2}NNO^{tBu}** suitable for X-ray diffraction were grown from slow vapour diffusion of diethyl ether into a dichloromethane solution of the ligand salt at −40 °C. The crystal structure of the ligand salt (Figure 4) reveals the coordination of two potassium ions within a centrosymmetric dimeric diamond core structure, involving two ligand molecules whose phenolic O atoms adopt a μ_2-bridging coordination mode. Each potassium ion is further stabilised by the coordination of the methoxy group from one ligand molecule and an imidazole group from the other ligand molecule. Each ligand molecule features one non-coordinated imidazole group. Coordination of a molecule of diethyl ether completes the overall pentacoordinate geometry of the potassium ion. Selected bond lengths and bond angles are given in Table S1. The C–O bond length of the phenolate is measured as 1.306(3) Å. This bond length is somewhat shortened compared to the C–O bond length of a neutral phenol (1.36 Å).

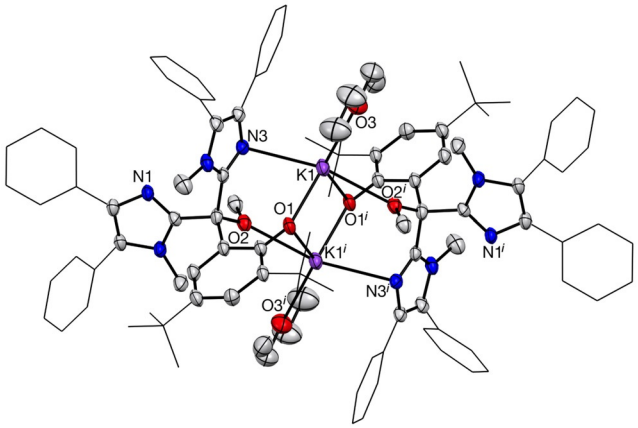

Figure 4. Displacement ellipsoid plot of [K_2(Im^{Ph2}NNO^{tBu})$_2$(OEt$_2$)$_2$] drawn at the 50% probability level. Only the major form of the disordered *t*Bu groups is drawn, Symmetry code *i*: 1−*x*, 1−*y*, 1−*z*. Hydrogen atoms and severely disordered solvent molecules are omitted for clarity. Ph and *t*Bu substituents of the imidazole and phenolate groups, respectively, are depicted in the wireframe format for clarity.

Synthesis and solid state characterisation of 1 and 2

The facial capping potential of anionic **Im^{Ph2}NNO^{tBu}** was investigated by exploring its coordination chemistry with Fe^{2+} and Zn^{2+}. Both iron and zinc complexes were prepared using analogous methods, depicted in Scheme 2. **K-Im^{Ph2}NNO^{tBu}** was dissolved in acetonitrile, and one equivalent of the desired metal(II) chloride precursor was added to the solution.[39] The mixture was stirred for two hours and was subsequently filtered and dried under vacuum. The crude solid was washed three times with hexane and was then dried under vacuum. The final reaction products were identified as mononuclear complexes [Fe(Im^{Ph2}NNO^{tBu})(Cl)] (**1**) and [Zn(Im^{Ph2}NNO^{tBu})(Cl)] (**2**), which were obtained in yields of 97% and 94%, respectively.

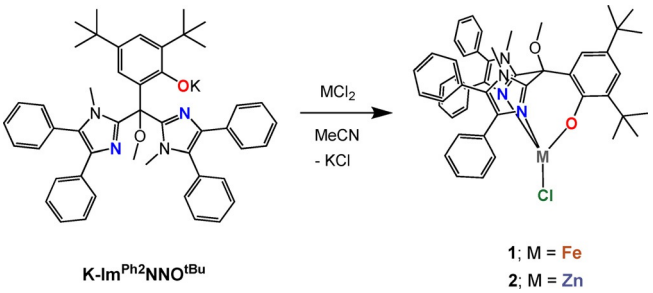

Scheme 2. Synthesis of [Fe(Im^{Ph2}NNO^{tBu})(Cl)] (**1**) and [Zn(Im^{Ph2}NNO^{tBu})(Cl)] (**2**).

IR analysis of both samples supports the anionic coordination of the phenolate ligand in each complex through the absence of an O–H stretching vibration. Solid-state zero-field ^{57}Fe Mössbauer analysis (80 K) of **1** produced a single quadrupole doublet with an isomer shift (δ) of 0.94 mm s^{-1} and a quadrupole splitting ($|\Delta E_Q|$) of 2.58 mm s^{-1}, consistent with high-spin ($S = 2$) iron(II) (Figure S22).

Crystals of **1** and **2** suitable for X-ray diffraction were grown from the slow vapour diffusion of *n*-hexane into a THF solution of each complex at ambient conditions. The crystal structures of complexes **1** and **2** are isostructural (Figure 5). Selected bond lengths and bond angles are given in Table 1 (below). In each complex, **Im^{Ph2}NNO^{tBu}** chelates to a single metal(II) ion by

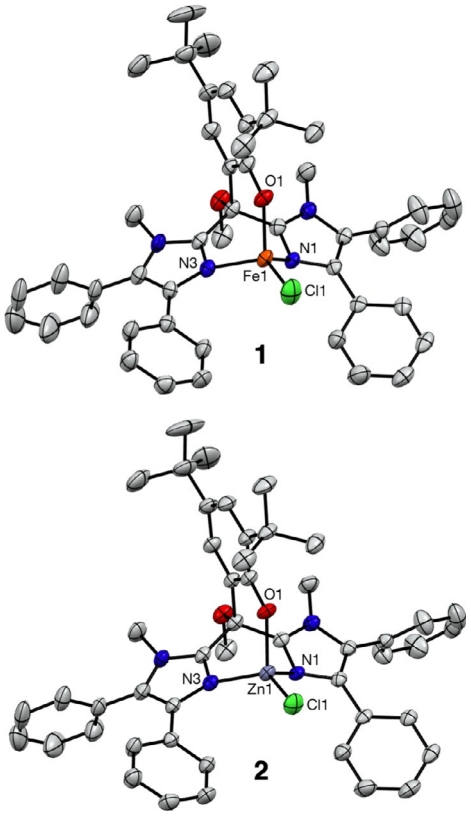

Figure 5. Displacement ellipsoid plots of **1** and **2** drawn at the 50% probability level. Only the major form of the disordered *t*Bu groups is drawn. Hydrogen atoms and severely disordered solvent molecules are omitted for clarity.

means of a tridentate *N,N,O* motif, involving both neutral imidazole N-donors and the anionic phenolate O-donor. The fourth coordination site is occupied by a chloride ligand, which completes the distorted tetrahedral geometry of each metal centre. Based on these results, **Im^{Ph2}NNO^{tBu}** can be regarded as a heteroscorpionate ligand that imparts a metallobicyclo[2.2.3]nonane topology to each complex. The ability of the ligand to monoligate is proposed to be principally due to the steric demands of its constituent groups, where the 4,5-diphenyl-substituted imidazole groups hinder the coordination of a second ligand equivalent and the *ortho*-*t*Bu substituent on the phenolate reduces the accessibility of the lone pair of the phenolic oxygen atom and prevents any bridging coordination modes from occurring.[23,28,35] Together, these bulky groups contribute to the relatively large buried volume of the ligand (58.9 and 59.6 % V_{buried} in **1** and **2**, Figure 6).

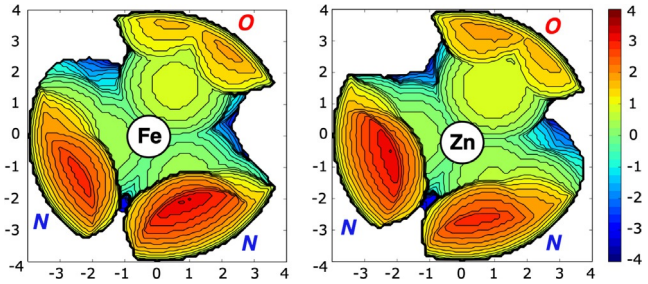

Figure 6. Steric maps of **Im^{Ph2}NNO^{tBu}** in **1** (left) and **2** (right) generated using the Samb*V*ca software.[40] Spheres are defined with a radius of 4 Å from the metal centre and H-atoms are included in the calculation.

The tetrahedral distortion in **1** and **2** is characterised by the N-M-O and N-M-N angles of the ligand being smaller than in the ideal tetrahedron, while the O-M-Cl and N-M-Cl angles are larger than ideal. This is due to the strain caused by the "cage" effect of the tripodal ligand scaffold, whose donor groups are linked by a single quaternary carbon atom, thereby imposing a certain degree of rigidity on the tripod and contracting the bite angles between its three donor atoms. The slightly elongated Fe–N bonds (> 2.0 Å) in **1** are consistent with the high spin nature of the iron(II) centre and lie within the range of Fe–N bond lengths previously obtained for other high spin non-heme iron(II) complexes bearing imidazole-derived *N,N,O* ligands.[31,41] The Fe1–O1 bond length of 1.8915(19) Å in **1** is relatively short and reflects the anionic nature of the phenolic oxygen atom. For comparison, an Fe–O bond length of 2.1979(14) Å was previously reported in our group for the pentacoordinate complex [Fe(BM^{Me}BIP^{nPr})(OTf)$_2$], whose supporting *N,N,O* ligand features a neutral *n*-propyl ester group.[31] Similarly, the Zn–N bond lengths in **2** fall well within the expected range for a zinc(II) nucleus of tetrahedral geometry bound to neutral N-donors.[26] The Zn1–O1 bond distance of 1.9266(12) Å in **2** is shorter than those reported by Burzlaff and co-workers for similar tetrahedral zinc complexes [Zn(bdtbpza)(Cl)] and [Zn(bpa^{tBu2,Me2})(CH$_3$)], featuring a carboxylate O-donor in the *N,N,O* ligand (1.990(2) and 2.054(6) Å, respectively).[26,34] This indicates a greater degree of charge localisation on the phenolate oxygen atom of **2** compared to a carboxylic acid oxygen donor.

In both complexes, the M–N bonds are observed to have slightly different lengths, contributing to the overall distortion of the tetrahedron. This asymmetry correlates with the different angles between the plane of the imidazole heterocycles and their respective M–N bond vectors (Figure 7). Angles of 146.13(13)° and 167.99(13)° are observed for C_{im}-N1-Fe1 and C_{im}-N3-Fe1 in **1**, which correspond to Fe–N bond lengths of 2.131(2) Å and 2.089(2) Å, respectively. In other words, the greater the distortion away from co-planarity, the longer the observed M–N bond length and the weaker the strength of the coordination bond. A similar phenomenon is observed for **2**. We attribute this effect to the inherent geometric restrictions imposed by the tripodal nature of the ligand, which force the metal out of plane relative to the imidazole rings and cause a slight twisting of the phenolate ring out of the approximate mirror plane.

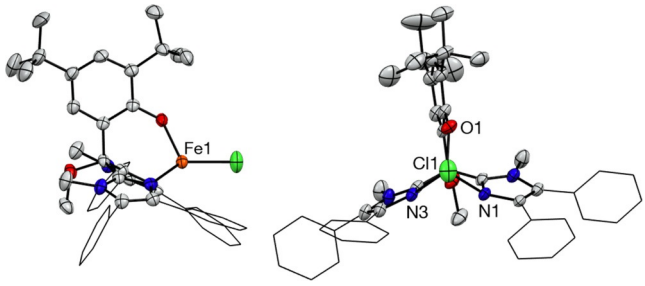

Figure 7. Views perpendicular (left) and parallel (right) to the Fe–Cl bond in the molecular structure of **1**. Displacement ellipsoids are drawn at the 50 % probability level. Phenyl substituents are drawn in the wireframe format for clarity.

To the best of our knowledge, **1** is one of only three crystallographically characterised mononuclear non-heme iron(II) complexes featuring a tripodal *N,N,O* ligand and that does not require additional stabilisation from an organic co-ligand. The tetrahedral nature of **1** differs somewhat from the typically penta- or hexacoordinate nature of enzymatic resting states that contain the 2H1C. A comparison of the geometric parameters of **1** with those of deacetoxycephalosporin C synthase (DAOCS, octahedral)[42] and 2,3-dihydroxybiphenyl dioxygenase (BphC, square pyramidal)[43] is given in Table 1. Overall, **1**

Table 1. Selected bond lengths and angles observed in the X-ray crystal structures of **1**, **2**, BphC (PDB 1EIL)[43] and DAOCS (PDB 1RXF).[42]

	1	**2**	BphC	DAOCS
Bond length [Å]				
M–N1	2.131(2)	2.0754(14)	2.24 (His_{145})	2.19 (His_{183})
M–N3	2.089(2)	2.0248(14)	2.30 (His_{209})	2.15 (His_{243})
M–O1	1.8915(19)	1.9265(12)	2.09 (Glu_{260})	2.15 (Asp_{185})
Angle angle [°]				
N1-M-O1	95.10(8)	95.91(5)	106.7	86.3
N3-M-O1	98.92(9)	100.97(5)	103.9	99.4
N1-M-N3	84.05(9)	88.23(5)	87.0	89.3

shows the greatest similarity to DAOCS, both in terms of the Fe–N bond lengths and the bond angles between the constituent atoms of the facial triad and the iron nucleus. However, the short Fe–O bond in **1** differs strongly from the Fe–O bond lengths in both enzymes, each of which is >2 Å (Figure 8).

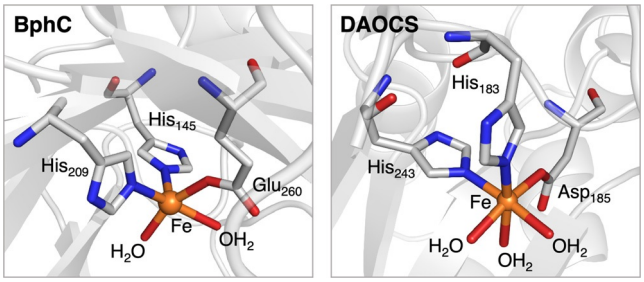

Figure 8. Active site structures of BphC from *Pseudomonas sp.* KKS102 (PDB 1EIL)[43] and DAOCS from *Streptomyces clavuligerus* (PDB 1RXF).[42] Carbon, iron, nitrogen and oxygen are depicted in grey, orange, blue and red, respectively.

Solution state behaviour of 2

In order to establish the rigidity of the $\mathbf{Im^{Ph2}NNO^{tBu}}$ ligand's tripodal *N,N,O* binding motif, we investigated the solution state behaviour of **2** in solvents of different binding affinities and varying steric bulk (CD_3CN, CD_2Cl_2, [D_8]THF, and [D_5]pyridine), using (variable temperature, VT) ^{1}H NMR and electronic absorption spectroscopy. In this way, the sensitivities of our newly developed biomimetic complexes can be elucidated, and further coordination chemistry can be controlled with greater precision.

The ^{1}H NMR analysis of **2** in various *deutero* solvents is depicted in Figure 9. One of the most noticeable features of this data-set is the similarity between the spectra recorded in CD_3CN and CD_2Cl_2, despite their different coordination affinities. In comparison, the spectra recorded in [D_8]THF or [D_5]pyridine are more complex and contain a larger number of peaks, possibly stemming from solvent-specific interactions or complex speciation in solution that arise from the sterically more demanding nature of these solvents.

The ^{1}H NMR spectrum of **2** in CD_3CN features two sharp singlets at 3.51 and 3.45 ppm, assigned to the *N*-methyl and *O*-methyl protons, respectively, of the supporting ligand framework. The 2:1 ratio of integral intensities is consistent with a metallobicyclo[2.2.3]nonane topology, indicating that the tripodal *N,N,O* coordination of $\mathbf{Im^{Ph2}NNO^{tBu}}$ is retained in solution. Analogous peaks at 3.52 and 3.45 ppm are observed in CD_2Cl_2, which show a high degree of structural similarity between the solute structure of **2** in acetonitrile and dichloromethane. Indeed, only minor differences are observed in the aromatic region of the spectra as well as the *tert*-butyl signals, which are ascribed to nonspecific solvent interactions. Strikingly, selective excitation of the *N*-methyl signal by means of 1D NOE NMR experiments in CD_3CN produced correlation signals to the *O*-methyl signal (3.45 ppm) as well as the *t*Bu signal (1.28 ppm), whereas selective excitation of OCH_3 did not produce any correlation response to the *t*Bu signals (Figure S45). In three-dimensional space, this places the methoxy group further away from the *t*Bu groups than the imidazole *N*-methyl groups,

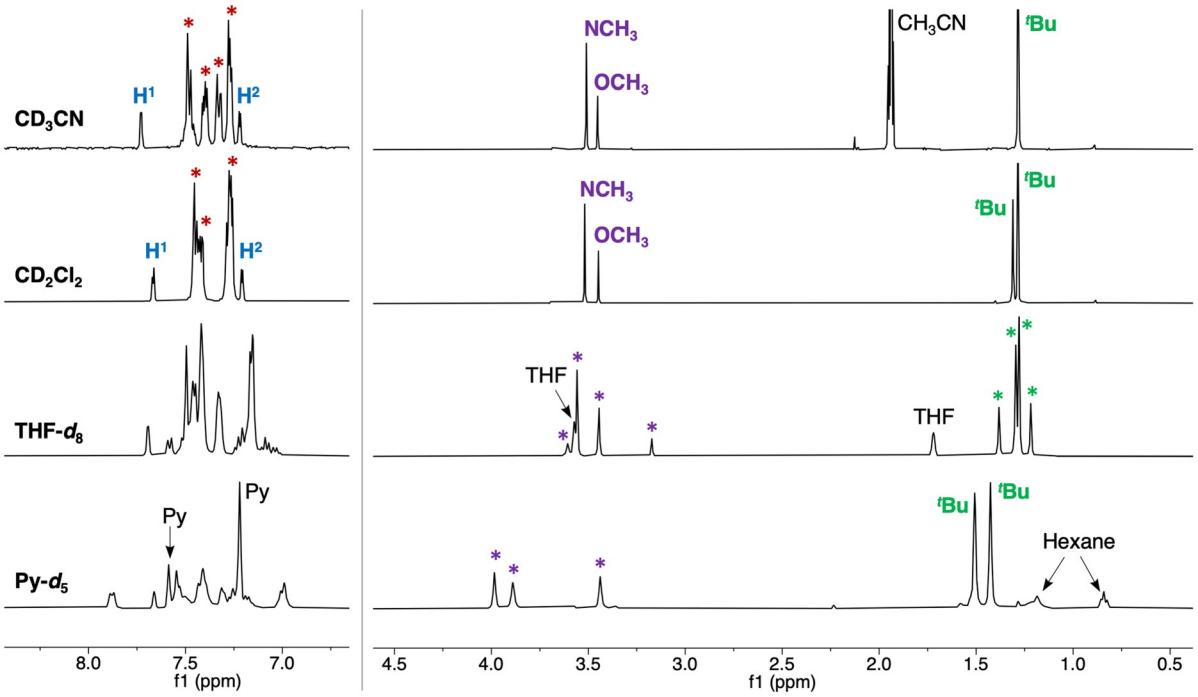

Figure 9. Stacked ^{1}H NMR (400 MHz) spectra of **2** in different *deutero* solvents, recorded at 298 K. The region between 4.5 and 6.5 ppm has been omitted for clarity and the signal intensity of the aromatic region has been amplified. Spectra are clipped vertically for clarity. Green asterisks indicate *t*Bu resonances. Purple asterisks indicate *N*-methyl and *O*-methyl resonances. Red asterisks denote aromatic protons on the phenyl groups. H^1 and H^2 are aromatic phenol ring protons.

which is in line with the observed H···H distances in the crystal structure (approximately 5.8 Å and 4.8 Å for the *O*-methyl and *N*-methyl groups, respectively). We therefore conclude that the solute structure of **2** in acetonitrile and dichloromethane is equivalent to its structure in the solid state. Additionally, VT ^{1}H NMR spectroscopy conducted in both CD_3CN and CD_2Cl_2 (Figure S46) demonstrates that no temperature-dependent fluxional processes occur in these solvents and that the structural integrity of **2** remains intact across a wide temperature range.

The ^{1}H NMR spectrum of **2** in [D_8]THF differs significantly from the previously discussed spectra. Most strikingly, four singlets are observed between 1.25 and 1.50 ppm in the region of the *tert*-butyl groups. The two central signals occur very close together at 1.30 and 1.28 ppm, which is similar in chemical shift to the *tert*-butyl resonances observed in CD_3CN and CD_2Cl_2. The two outer singlets at 1.38 and 1.22 ppm have equal integral values, and together have a 1:2 integral ratio relative to the two large singlets. Overall, this would suggest that two species are present in solution. Further evidence to support this can be found in the spectral region between 3.10 and 3.70 ppm associated to the *N*-methyl and *O*-methyl groups, where four signals are observed instead of the expected two. In addition, the aromatic region of the spectrum is very disordered, which also suggests that multiple species may be present in solution. Over the course of several days, the relative intensities and chemical shifts of these different NMR signals do not change. Similarly, the spectrum remains unchanged after cooling or heating the sample and repeating the measurement at room temperature, suggesting that the two species present in THF solution are in thermal equilibrium. VT NMR spectroscopy of **2** in [D_8]THF reveals a temperature-dependent fluxional process that occurs on the NMR time-scale (see Figure S47). This is most pronounced in the region around 3.5 ppm where two signals are seen to coalesce as the temperature increases. Another important observation is the appearance of a small shoulder at 1.75 ppm next to the residual [D_8]THF peak at low temperature. This suggests that the solvent participates in the coordination equilibrium, possibly through direct coordination to the metal centre. By coordinating to the metal, it is hypothesised that THF could initiate the dissociation of one of the two imidazoles.

Dissolving **2** in [D_5]pyridine produces a yellow solution, whose ^{1}H NMR spectrum indicates that a disruption in the complex symmetry has taken place. This is most clearly identified by the presence of three singlets at 3.98, 3.89 and 3.44 ppm, each with an integral value of 3 H. This suggests that the imidazole groups no longer coordinate to the metal ion in an equivalent manner. Slow diffusion of hexane into a pyridine solution of **2** under ambient conditions resulted in the formation of yellow needles that were identified as the simple $[Zn(Cl)_2(py)_2]$ complex, which is known from the literature.[44] Based on this data, we hypothesise that the strongly coordinating and sterically demanding nature of pyridine disrupts the *N,N,O* coordination of **Im^{Ph2}NNO^{tBu}** and enables pyridine to scavenge a portion of the available zinc. This causes a mixture of decomposition products to form, possibly including a bis-ligated compound of the type $[Zn(Im^{Ph2}NNO^{tBu})_2]$ (vide infra).

Solution state behaviour of 1

By analogy to **2**, complex **1** is expected to retain the same structure in acetonitrile and dichloromethane solution. Using Evans' NMR method,[45] the magnetic moment of **1** in CD_3CN was determined to be 4.50 BM, which corresponds to a high-spin ($S = 2$) electronic configuration and is consistent with the solid state geometry and Mössbauer parameters previously described. The ^{1}H NMR spectra of **1** in CD_3CN and CD_2Cl_2 contain paramagnetically shifted signals (Figure 10), and certain resonances are observed to have almost identical chemical shifts in both solvents (e.g. the signals at 58, 50 and 10 ppm). This supports the assumption that the hyperfine interactions between protons of the ligand scaffold and the paramagnetic iron centre are similar in both solvents. However, additional broad signals are observed in CD_3CN (e.g. the signals at 51, 36, 33, and 23 ppm) that are not present in CD_2Cl_2. VT ^{1}H NMR analysis of **1** in both solvents showed normal Curie behaviour with highly linear Curie plots (Figure 10) that converge to the diamagnetic region upon extrapolation to infinite temperature, thereby excluding the presence of any spin crossover phenomena or reversible solvent coordination in solution (see Figures S28–S31). This suggests that the differences between the ^{1}H NMR spectra may simply arise from the different solvent-specific effects. Moreover, the electronic absorption spectra of **1** in CH_3CN and CH_2Cl_2 are almost identical, featuring a very weak, broad band at approximately 500 nm as well as a broad band at 380 nm that shoulders the intense ligand-based π–π^* transitions ($<$350 nm). The UV/Vis spectrum of **1** in CH_3CN displays no temperature dependence within the range of 298–233 K (Figure S34).

Unlike **2**, the ^{1}H NMR spectrum of **1** in [D_8]THF does not reveal the presence of multiple species in solution at 298 K. Indeed, the UV/Vis spectrum of **1** in THF is very similar to those recorded in CH_3CN and CH_2Cl_2, which suggests that an electronically similar species is present in solution. However, conducting VT ^{1}H NMR analysis in [D_8]THF reveals more deviation from ideal Curie behaviour, which is indicative of additional processes occurring in solution at low temperature (Figures S32 and S33). Recording a ^{1}H NMR spectrum at 298 K after having either cooled or heated the sample produced the same spectrum as that recorded prior to any temperature change. This suggests that a reversible solvent-related coordination equilibrium in THF solution occurs. Similarly to **2**, dissolving complex **1** in [D_5]pyridine produces a yellow solution (λ_{max} = 420 nm), indicating the formation of a $FeCl_2$-pyridyl adduct in solution.[46,47] Moreover, the paramagnetic ^{1}H NMR spectrum of **1** in [D_5]pyridine contains fewer peaks and bears little resemblance to the spectra recorded the other *deutero* solvents, which suggests that a new species has formed in solution.

Slow vapour diffusion of *n*-hexane into a pyridine solution of **1** resulted in the growth of needle-like pale yellow crystals that were suitable for X-ray diffraction. The resulting crystal structure reveals the formation of a mononuclear, bis-ligated com-

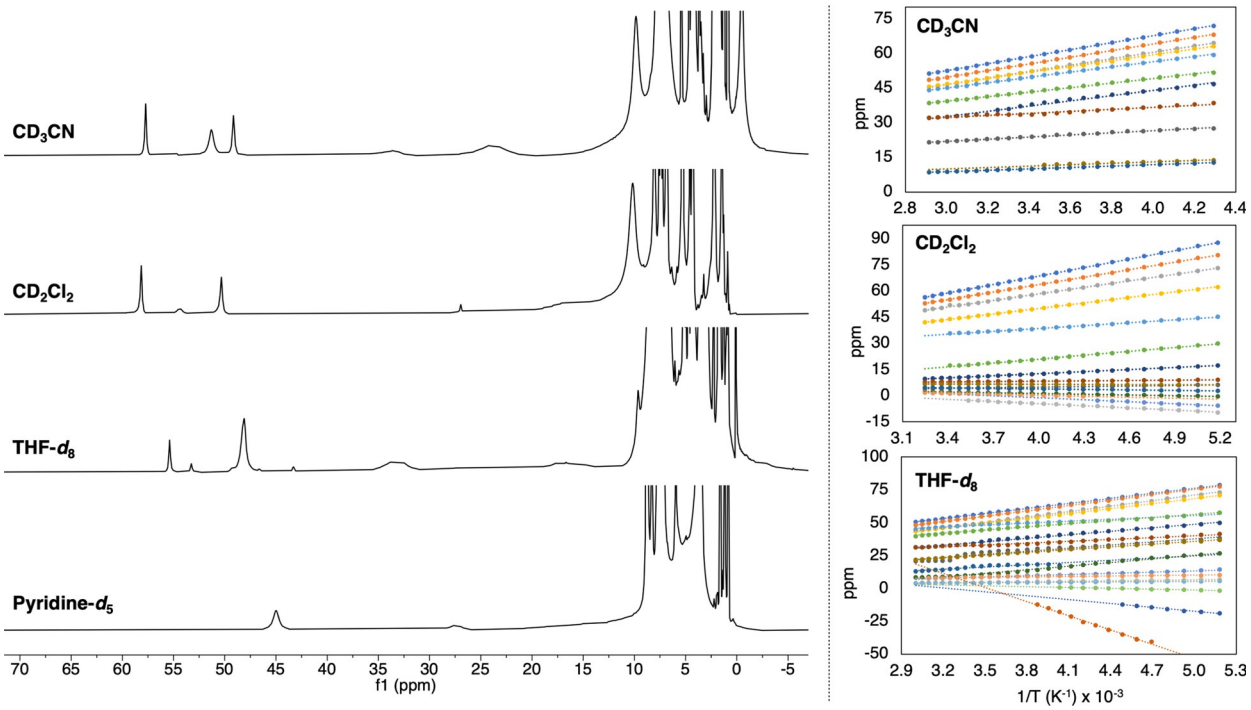

Figure 10. Left: stacked paramagnetic ^{1}H NMR (400 MHz) spectra of **1** in different *deutero* solvents, recorded at 298 K. Spectra have been clipped for clarity. Right: Curie plots showing the inverse temperature dependence of the paramagnetic ^{1}H NMR chemical shifts (ppm) for **1** in CD_3CN, CD_2Cl_2 and [D_8]THF.

plex, [Fe($\kappa_{N,O}$-Im^{Ph2}NNO^{tBu})$_2$] (**3**) (Figure 11). Selected bond lengths and bond angles are given in Table S4. The iron centre has a distorted tetrahedral geometry, bound by two ligand molecules, each of which chelates by means of a new bidentate *N,O* coordination mode involving the anionic phenolic oxygen atom and a neutral imidazole N-donor. The second imidazole group is unbound, orientated away from the iron in such a way that the methoxy group is forced into relatively close proximity to the metal (Fe1···O21 and Fe1···O22 distances of 2.4598(18) and 2.513(2) Å, respectively). This result confirms the disrupting effect that pyridine has on the tripodal coordination of **Im^{Ph2}NNO^{tBu}**.

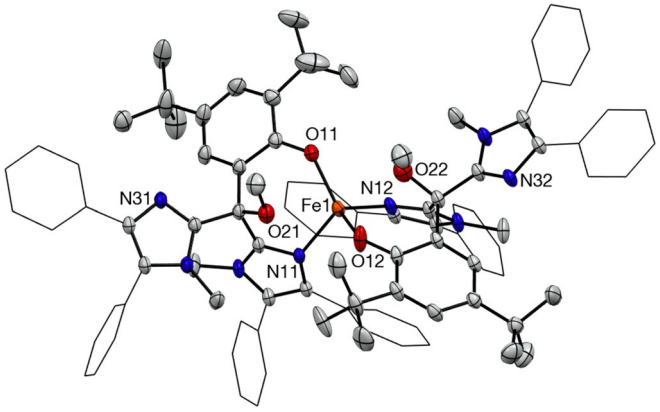

Figure 11. Displacement ellipsoid plot of **3** drawn at the 50% probability level. Only the major form of the disordered *t*Bu group is drawn. Hydrogen atoms, non-coordinated pyridine molecules and severely disordered solvent molecules are omitted for clarity. Phenyl substituents are depicted in the wireframe format for clarity.

Synthesis of a zinc thiolate complex (4)

The substitutional lability of the chloride ligand in **2** was investigated using a monodentate thiophenolate. Complex **2** was dissolved in CH_2Cl_2 and a slight excess of NaSPh was added. The reaction mixture stirred 3 h and was subsequently filtered and dried under vacuum. The crude solid was washed with hexane and dried under vacuum, affording [Zn(Im^{Ph2}NNO^{tBu})(SPh)] (**4**) in 95% yield (Scheme 3). Crystals suitable for X-ray diffraction were grown from slow vapour diffusion of *n*-hexane into a THF solution of **4** at room temperature.

The crystal structure of **4** (Figure 12) reveals the formation of a mononuclear zinc(II) complex with a distorted tetrahedral geometry. Selected bond lengths and bond angles are given in Table S5. **Im^{Ph2}NNO^{tBu}** has retained its *N,N,O* binding mode involving both neutral imidazole N-donors and the anionic phenolic O-donor. The ligand's buried volume in **4** is calculated as

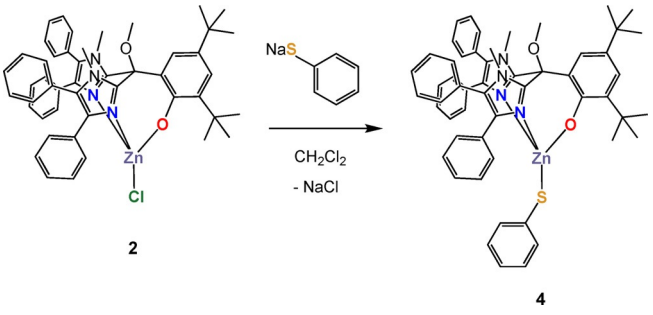

Scheme 3. Synthesis of [Zn(Im^{Ph2}NNO^{tBu})(SPh)] (**4**).

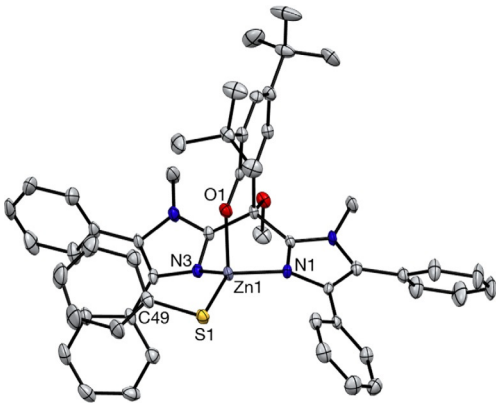

Figure 12. Displacement ellipsoid plot of **4** drawn at the 50% probability level. Hydrogen atoms and disordered THF molecules are omitted for clarity.

59.4% V_{buried}, which is almost identical to that in **2**. The thiophenolate binds through its anionic sulfur atom to the zinc's fourth coordination site. The Zn1-S1-C49 angle of 101.67(11)° is typical for an arylthiolate coordinated to a transition metal and the Zn–S bond length of 2.2249(9) Å is comparable to those reported for other tetrahedral zinc(II) thiophenolate complexes (2.2201(13)–2.418(1) Å).[48–54] Similarly to **2**, the tetrahedral distortion in **4** is characterised by N-Zn-O and N-Zn1-N angles that are significantly smaller than the ideal tetrahedron angle, and N-Zn-S and O-Zn-S angles that are larger than 109.5°. Interestingly, the thiolate appears to be coordinated in such a way that its aryl substituent "bends" towards one of the two imidazole groups, effectively imparting chirality to the complex. However, the overall crystal structure of **4** must be considered racemic as can be seen by the centrosymmetric space group (Figure 13). Overall, the low coordination number, the single metal–sulfur bond, and the facial *N,N,O* triad qualify **4**

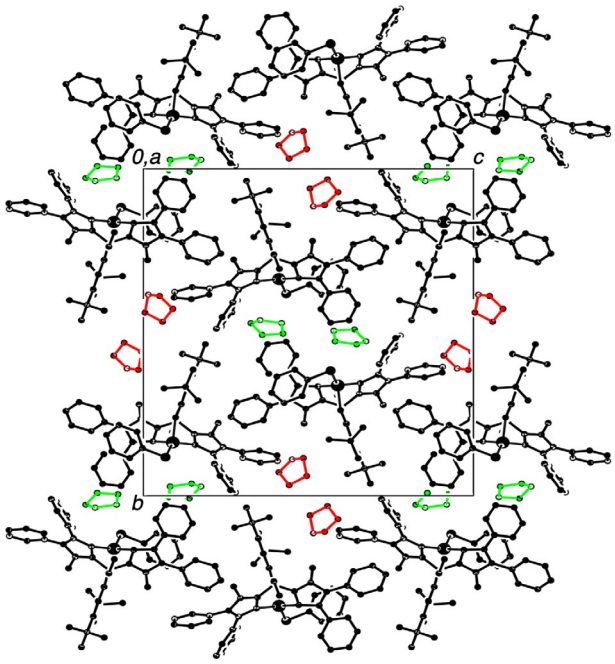

Figure 13. Packing of **4** in the crystal, shown along the *a*-axis. H-atoms are omitted for clarity. Two independent THF molecules in the asymmetric unit are depicted in red and green. Only the major form of the disordered THF is shown.

as an accurate (diamagnetic) structural model of the ACV-bound active site of IPNS.

Solution state behaviour of 4

The ^{1}H NMR spectrum of **4** in different *deutero* solvents is depicted in Figure 14. The ^{1}H NMR spectra of **4** in CD_3CN and

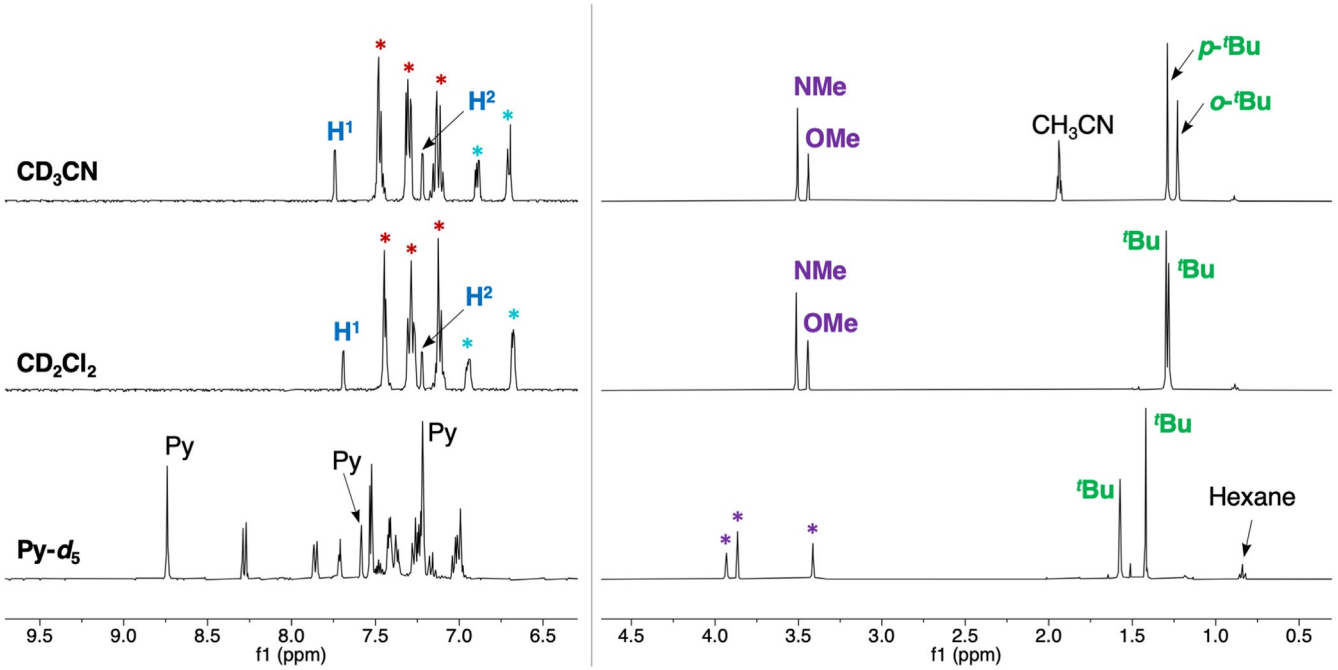

Figure 14. Stacked ^{1}H NMR (400 MHz) spectra of **4** in different *deutero* solvents, recorded at 298 K.

CD_2Cl_2 both feature sharp singlets at 3.51 ppm and 3.44 ppm, assigned to the *N*-methyl and *O*-methyl groups of the supporting ligand framework, respectively. Their relative integral ratio of 2:1 supports the metallobicyclo[2.2.3]nonane topology associated to the facial binding motif of the **Im^{Ph2}NNO^{tBu}** ligand. In both spectra, the thiolate ligand can be identified by the presence of two multiplets in the aromatic region of the spectra, the most deshielded being assigned to the two protons *ortho* to the sulfur atom. Interestingly, the chemical shifts of the phenolic protons have not changed compared to those of **2**, which suggests that chloride substitution for the thiophenolate does not have a significant impact on the electronic properties of the phenolate ring. VT ^{1}H NMR analysis in CD_3CN and CD_2Cl_2 (see Figures S57 and S58) demonstrates that **4** retains its structural integrity across a wide temperature range, as neither fluxional behaviour of the supporting ligand nor any thiophenolate dissociation was observed in either solvent. Finally, 1D NOE ^{1}H NMR experiments in CD_3CN confirmed the three-dimensional structure of **4** as being the same in solution as it is in the solid state (see Figures S55 and S56).

Dissolving **4** in [D_5]pyridine produced a pale pink solution whose ^{1}H NMR spectrum reveals a number of significant changes compared to the spectra obtained in CD_3CN and CD_2Cl_2. Most importantly, three singlets are observed at 3.93, 3.87, and 3.41 ppm, each with a relative integral of 3 H. This strongly suggests that the supporting ligand's facial binding motif has been disrupted and that a break in symmetry has occurred. Furthermore, a significant increase in the number of observed aromatic signals has occurred, which is in accordance with both imidazole groups having different chemical environments. Colourless crystals suitable for X-ray diffraction were grown from slow vapour diffusion of hexane into a pyridine solution of **4** at room temperature. The resulting crystal structure reveals the formation of a new complex, [Zn(Im^{Ph2}NNO^{tBu})(SPh)(py)] (**5**), where direct coordination of a pyridine molecule to the zinc centre has taken place (Figure 15). This has caused the zinc's coordination environment to expand from four- to five-coordinate, and has also lead to a disruption of the *N*,*N*,*O* coordination of **Im^{Ph2}NNO^{tBu}**. The steric demands of the pyridine ligand have caused one of the imidazole groups of the supporting ligand to dissociate, resulting in a closer proximity of the methoxy group to the zinc ion. This results in the coordination of the supporting ligand by means of an alternative facial *N*,*O*,*O* coordination mode to the zinc metal centre, comprising an anionic phenolic O-donor, one of the neutral imidazole N-donors and the loosely bound neutral methoxy O-donor (Zn1–O2 distance of 2.455(3) Å). Selected bond lengths and bond angles are given in Table S6.

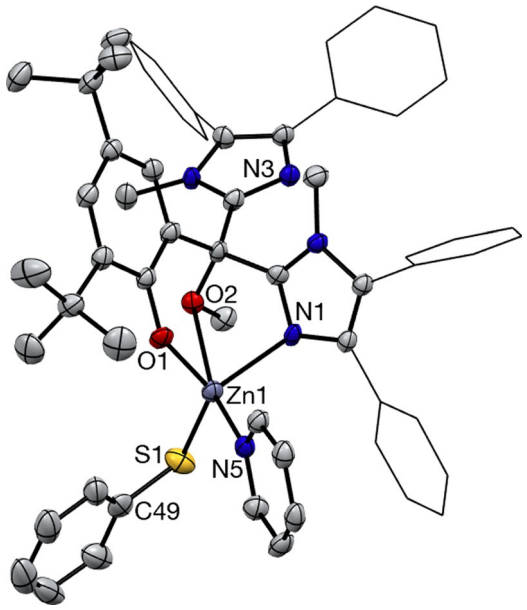

Figure 15. Displacement ellipsoid plot of **5** drawn at the 50% probability level. Hydrogen atoms and partially occupied non-coordinated pyridine molecules are omitted for clarity. Phenyl substituents are depicted in the wire-frame format for clarity.

Electrochemistry

Phenolate ligands are known to be redox non-innocent in character, which prompted us to investigate the electrochemical properties of complexes **1**, **2** and **4**, and examine the effect of combining the redox non-innocent character of the supporting ligand with zinc (redox inert), iron (redox non-innocent), as well as a redox non-innocent thiophenolate ligand. The redox properties of the complexes were investigated by cyclic voltammetry (CV) under an inert N_2 (g) atmosphere in acetonitrile, using [nBu$_4$N]PF$_6$ as a supporting electrolyte. All quoted potentials are referenced versus the ferrocene/ferrocenium couple (Fc/Fc$^+$). The redox behaviour of the ligand salt was investigated for comparison. The voltammograms are displayed in Figure 16.

Scanning across the potential range of −2.1 V to +1.1 V, the voltammogram of **K-Im^{Ph2}NNO^{tBu}** features a strong oxidation wave, **A** ($E_{p,a}$ = +0.46 V), that we ascribe to the phenolate oxidation to its phenoxyl form.[55–57] This is approximately 0.5 V lower compared to the oxidation potential of tri-substituted

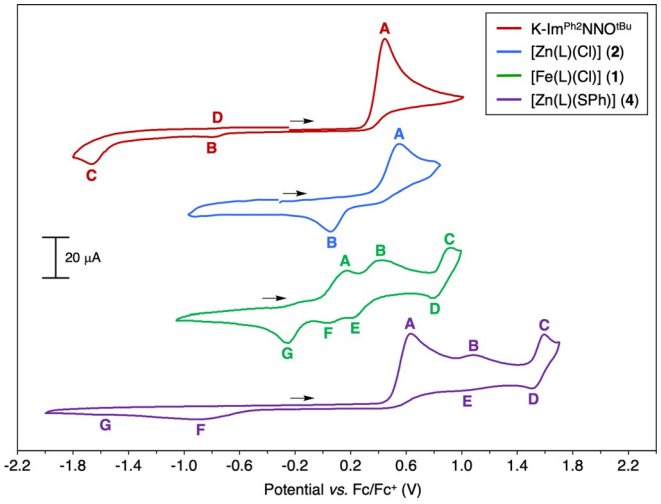

Figure 16. Cyclic voltammograms of **K-Im^{Ph2}NNO^{tBu}**, **2**, **1** and **4**, recorded in a 0.1 M solution of [nBu$_4$N]PF$_6$ in acetonitrile at ambient temperature and with a scan rate of 100 mV s^{-1}.

phenols such as 2,4,6-tri-*tert*-butylphenol or 2,4,6-trimethylphenol that oxidize at ca. 1.0 V (vs. Fc/Fc^+),[58,59] which reflects the anionic state of the phenolic oxygen atom in **K-Im^{Ph2}NNO^{tBu}**. A reduction event, **C** ($E_{p,c} = -1.66$ V), is observed that only occurs after **A** has taken place (see Figure S71), prompting us to assign it to the electrochemical reduction of the phenoxyl radical. The large peak separation between **A** and **C** (ca. 2 V) and the relatively diffuse nature of both signals reflects the highly irreversible nature of this redox couple and is consistent with previous observations made for the electrochemical behaviour of substituted phenols in coordinating solvents.[58,59] Moreover, the structure of the ligand salt in solution is likely very dynamic, involving imidazole lability, solvent coordination to the potassium ion and possible coordination equilibria between monomeric and dimeric states, all of which contribute to the diffuse and irreversible nature of the electrochemical events. The electrochemical responses **B** and **D** (that occur at approximately −0.75 V) are very minor and become less well defined at higher scan rates (Figure S70). We therefore tentatively ascribe them either to the presence of small amounts of structural isomers or to the presence of a minor impurity.

The voltammogram of complex **2** features a single irreversible redox couple within the potential range of −1.0 V to +0.8 V with the oxidation (**A**) and reduction (**B**) occurring at $E_{p,a} = +0.56$ V and $E_{p,c} = +0.07$ V, respectively. Given the redox-inert nature of divalent zinc, these electrochemical responses are assigned as phenolate-based electron transfers. The phenolate oxidation potential is comparable to that of other zinc(II) phenolate complexes bearing mixed N,O-donor ligands.[60,61] Compared to the ligand salt, the phenolate oxidation in **2** has undergone a 100 mV anodic shift. This is likely due to a depletion in the electron density on the phenolate's oxygen atom as a result of its coordination to the Lewis acidic zinc ion.[62] Additionally, we ascribe the smaller peak-to-peak separation of **A** and **B** in **2** (compared to **A** and **C** in **K-Im^{Ph2}NNO^{tBu}**) to the rigid, tripodal coordination of the ligand to zinc in acetonitrile solution, which may help to increase the (electro)chemical reversibility of the phenolate-centred electron transfers. Scanning beyond +0.85 V, additional irreversible oxidations were observed with no reduction events taking place on the return scan, indicating decomposition of the complex on the surface of the working electrode.

The presence of a redox-active metal in **1** produces a voltammogram of greater complexity than that of **2**, with three oxidative waves (**A**–**C**) and four reductive responses (**D**–**G**) observed within the potential range of −1.0 V and +1.0 V. The voltammogram is reproducible over at least 20 cycles, which implies that the electrochemical cycle it represents is overall chemically reversible. The first oxidation event, **A** ($E_{p,a} = +0.18$ V) is assigned to iron oxidation on the basis of its low oxidation potential. It forms an irreversible redox couple to **G** ($E_{p,c} = -0.25$), which suggests that the formation of a ferric ion is accompanied by additional chemical or structural changes in solution. One possibility is that the preference for an octahedral geometry may drive the ferric ions into coordination equilibria with acetonitrile, deviating from the original tetrahedral geometry of the complex. Indeed, this is reflected by the diffuse nature of the subsequent oxidation, **B** ($E_{p,a} = +0.42$ V), ascribed to phenolate oxidation.[63] By means of segmentation experiments (Figure S74), **B** was shown to be redox-coupled to both **E** (+0.23 V) and **F** (+0.04 V), supporting the hypothesis that a mixture of species is present in solution after the initial oxidation event **A**. Finally, a quasi-reversible redox couple comprising **C** and **D** ($E_{1/2} = +0.88$ V) is observed that we tentatively assign to a Fe^{IV}/Fe^{III} couple, based on similar potentials reported for other non-heme iron complexes supported by tripodal ligands.[64,65]

Substitution of the chloride ligand in **2** for the thiophenolate ligand in **4** can be regarded as the addition of a redox centre within the zinc complex framework. Scanning oxidatively, a strong irreversible oxidation, **A** ($E_{p,a} = +0.65$ V), is observed that is followed by a second more diffuse oxidation, **B** ($E_{p,a} = +1.07$ V). We ascribe these to the sequential oxidation of the phenolate and thiophenolate moieties, on the basis of literature precedents.[56,62,66] The presence of the thiolate ligand has therefore caused the phenolate oxidation to shift anodically by approximately 0.1 V compared to **2**. Scanning beyond +1.4 V, a quasi-reversible redox couple is observed, **C** and **D** ($E_{1/2} = +1.57$ V), which we assign to a ligand-centred electron transfer, although we are unable to assign it definitively to the thiolate or to the phenolate. Reduction **F** ($E_{p,c} = -0.89$ V) was observed not to occur without **A** having previously taken place (Figure S78), which prompted our assignment of **F** to the phenoxide reduction. Interestingly, segmentation experiments revealed that **F** is less broad when **C** has not taken place (Figure S79), demonstrating that sequential electrochemical oxidations of **4** provoke structural changes in solution that increase the activation energy required for **F**. Presumably, these structural changes account for the overall irreversibility of the electrochemical events.

Overall, these results demonstrate the redox non-innocence of **Im^{Ph2}NNO^{tBu}** and show that phenolate oxidation is the first electrochemical response observed upon subjecting **K-Im^{Ph2}NNO^{tBu}**, **2** and **4** to oxidative conditions. The thiolate ligand in **4** is slightly more difficult to oxidise than phenolate, which suggests that its soft nature may help create more covalent bonds with transition metals than the phenolic oxygen, thereby reducing its charge localisation and rendering it less prone to oxidation. Moreover, the 2,4-disubstitution of the phenolate group helps stabilise the phenoxyl radical and make its formation more thermodynamically favourable. The cyclic voltammogram of **1**, however, is more difficult to interpret due to the redox non-innocent nature of both the iron and the phenolate. A more definitive assignment of these electrochemical processes has been made by means of computational studies.

Computational studies

In order to better understand the electronic structures of complexes **1**, **2** and **4**, we resorted to density functional theory (DFT) calculations. For ease of comparison, we also performed DFT calculations on the theoretical monomeric structure of the ligand's potassium salt (**K-L^{opt}**), where a tripodal *N*,*N*,*O* ligand

binding mode to the potassium cation has been imposed. Overall, the geometries (**1**^{opt}, **2**^{opt} and **4**^{opt}) obtained from the gas-phase geometry optimisations are consistent with the X-ray crystal structures. The electron density was subsequently recalculated at the B3LYP/6-311g(d,p) level of theory. For **K-L**^{opt}, **2**^{opt} and **4**^{opt}, the energies of the Kohn–Sham molecular orbitals (MOs) were extracted from these geometries. The α and β MOs in **1**^{opt}, were biorthogonalised with the Multiwfn program,[67] using the Fock matrix from natural bonding orbital (NBO) analysis in order to evaluate their energies. The MO energies calculated for **K-L**^{opt}, **1**^{opt}, **2**^{opt} and **4**^{opt} are given in Table S7 and are depicted schematically in Figure 17. The MO energies for **1**^{opt} have been ordered according to the average energy of the α and β orbitals generated upon biorthogonalization.

Our calculations show that the HOMO in **K-L**^{opt}, **2**^{opt} and **4**^{opt} is consistently localised on the phenolate group. This demonstrates clearly that **Im**^{Ph2}**NNO**^{tBu} has redox non-innocent character and supports our assignment of the first electrochemical oxidation of these compounds as being ligand-centred. The calculations also show that the HOMO in **K-L**^{opt} (−4.26 eV) is more energetically accessible than that in **2**^{opt} and **4**^{opt}, which reflects the electronic effect imparted by the more Lewis acidic zinc centre. In contrast, the HOMO in **1**^{opt} is localised on the iron centre and lies much higher in energy than for the other complexes. Indeed, the occupied MOs of highest energy in **1**^{opt} are calculated as being the five iron d-orbitals, four of which are singly occupied and one of which is filled. NBO calculations also show the natural spin density to be almost entirely localised on the iron centre (Figure 17 and Table S8). Together, these calculations indicate that the ferrous centre in **1** is most prone to oxidation despite the redox-active nature of the phenolate group, and support our assignment of the first electrochemical oxidation in **1** to the Fe^{II}/Fe^{III} oxidation.

Computations also reveal that the HOMOs in **2**^{opt} and **4**^{opt} are similar in energy (−4.97 eV and −4.84 eV, respectively), thereby supporting the hypothesis that the oxidation potential of the supporting phenolate is not significantly affected by the exogenous ligand substitution on the zinc centre. Similarly, the presence of a thiolate ligand in **4**^{opt} has no effect on the energy of the LUMO compared to **2**^{opt}. We attribute this to the highly aromatic character of the LUMO, which is delocalised across the bis-imidazole ligand backbone in both cases and is,

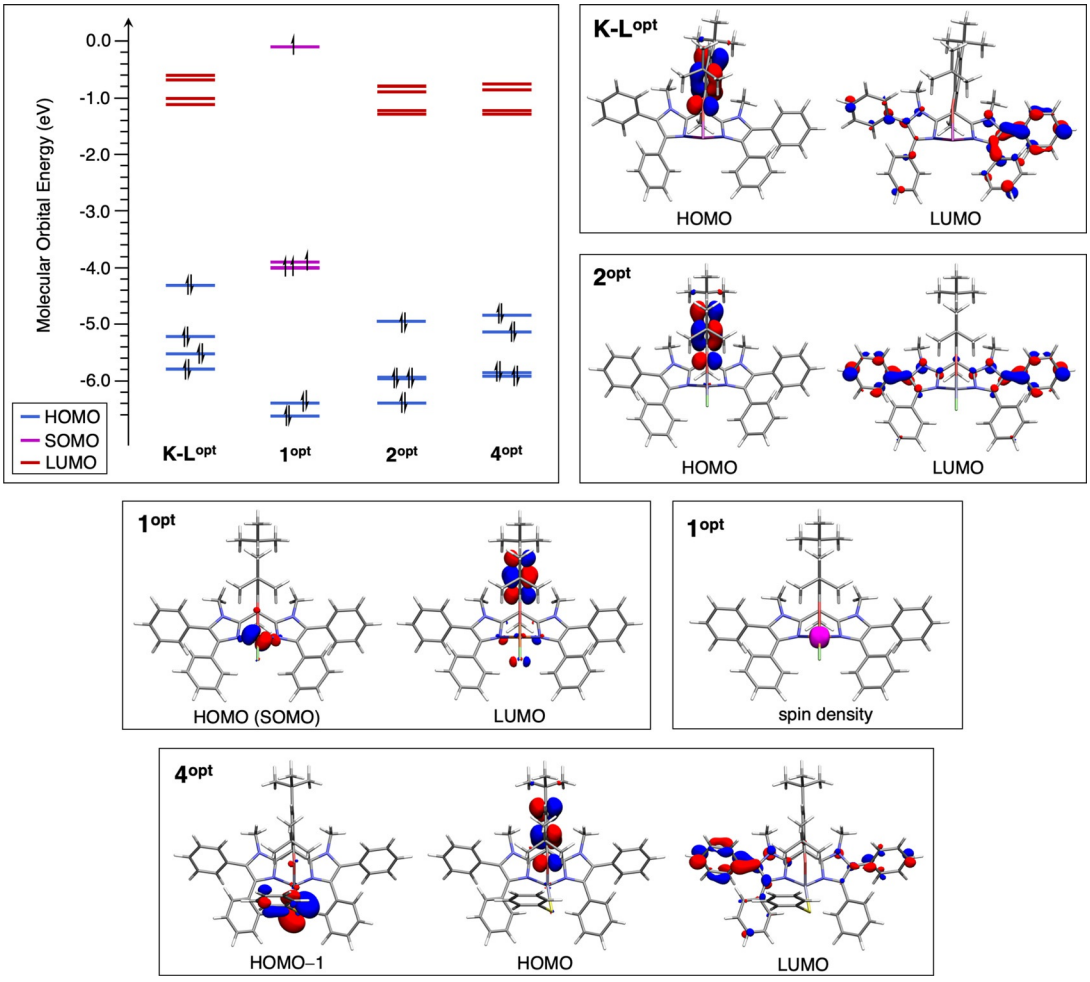

Figure 17. Calculated MO energies for **L-K**^{opt}, **1**^{opt}, **2**^{opt} and **4**^{opt}. LUMOs for **1**^{opt} are not depicted as they occur higher in energy than the given scale. Relevant MO diagrams for each complex are also provided (isosurface: ±0.05). HOMO: highest occupied molecular orbital; LUMO: lowest unoccupied MO; SOMO: singly occupied MO.

presumably, highly energetically inaccessible. Finally, the HOMO−1 in $\mathbf{4}^{opt}$ is calculated as being localised on the sulfur atom, which indicates that the thiolate is slightly less prone to oxidation than the phenolate and supports our assignment of the sequential oxidations in the CV of **4**.

Conclusions

This work has established $\mathbf{Im^{Ph2}NNO^{tBu}}$ as a synthetically accessible, bioinspired ligand that can structurally model the 2H1C by means of a facial *N,N,O* binding motif. Reacting **K-$\mathbf{Im^{Ph2}NNO^{tBu}}$** with iron(II) or zinc(II) chloride afforded the isostructural complexes [Fe($Im^{Ph2}NNO^{tBu}$)(Cl)] (**1**) and [Zn($Im^{Ph2}NNO^{tBu}$)(Cl)] (**2**) in high yield. These complexes can be regarded as highly convenient synthons from which a range of biomimetic complexes bearing biorelevant co-ligands could be created. In this work, the substitutional lability of the chloride ligand in **2** was investigated using a simple thiophenolate ligand, producing complex [Zn($Im^{Ph2}NNO^{tBu}$)(SPh)] (**4**) in high yield. The low coordination number, the single metal–sulfur bond, and the facial *N,N,O* supporting ligand qualify **4** as an accurate (diamagnetic) structural model of the substrate-bound IPNS active site. Detailed investigation of the solution state behaviour of **1**, **2**, and **4** showed that the complexes retained their structural integrity in acetonitrile and dichloromethane solutions, while coordinating solvents of greater bulk such as THF and pyridine provoke structural rearrangements and lead to alternative bidentate (κ_2-*N,O*) and tridentate (κ_3-*N,O,O*) coordination modes of the supporting ligand. Having elucidated the sensitivities and solution-state dependencies of $\mathbf{Im^{Ph2}NNO^{tBu}}$, this ligand has now been established as a robust platform from which to structurally model the 2H1C bioinorganic motif. Cyclic voltammetry studies, supported by DFT calculations, demonstrated the redox non-innocence of $\mathbf{Im^{Ph2}NNO^{tBu}}$ as phenolate oxidation was the first electrochemical response observed in **K-$\mathbf{Im^{Ph2}NNO^{tBu}}$**, **2** and **4**. However, the initial electrochemical oxidation of **1** was shown to occur at the iron centre and not at the phenolate. Therefore, **1** is an interesting complex with which to investigate the spectroscopy and oxidative transformations of derivative iron complexes that model 2H1C-containing iron enzymes. Our group currently focuses on the development of mononuclear non-heme iron thiolate complexes that structurally model the substrate-bound active site of IPNS.

Acknowledgements

Financial support was provided by the European Union through the Marie Sklodowska-Curie NoNoMeCat ITN network (675020-MSCA-ITN-2015-ETN). The X-ray diffractometer was financed by the Netherlands Organisation for Scientific Research (NWO). This work was sponsored by NWO Exacte en Natuurwetenschappen (Physical Sciences) for the use of supercomputer facilities, with financial support from NWO. S.Y. gratefully acknowledges the financial support from the Max-Planck Society, in particular, the joint workspace of the Max-Planck Institute for Chemical Energy Conversion (MPI-CEC) and the Max-Planck Institute for Coal Research (MPI-KOFO). We are very grateful to Dr. Marc-Etienne Moret and Dr. Danny Broere for their valuable input during scientific discussions. We would like to express our gratitude to Dr. Eckhard Bill and Bernd Mienert of the MPI-CEC for help with the acquisition of the Mössbauer data and for the fruitful discussions. We thank Dr. Johann Jastrzebski for assistance with NMR measurements and Serhii Tretiakov for assistance with the MO calculations and visualisations.

Conflict of interest

The authors declare no conflict of interest.

Keywords: 2-His-1-carboxylate facial triad · bioinspired · enzyme models · *N,N,O* ligand · non-heme iron

[1] S. J. Lange, L. Que, Jr., *Curr. Opin. Chem. Biol.* **1998**, *2*, 159 – 172.
[2] E. L. Hegg, L. Que, Jr., *Eur. J. Biochem.* **1997**, *250*, 625 – 629.
[3] L. Que, Jr., *Nat. Struct. Biol.* **2000**, *7*, 182 – 184.
[4] M. Costas, M. P. Mehn, M. P. Jensen, L. Que, Jr., *Chem. Rev.* **2004**, *104*, 939 – 986.
[5] P. C. A. Bruijnincx, G. Van Koten, R. J. M. Klein Gebbink, *Chem. Soc. Rev.* **2008**, *37*, 2716 – 2744.
[6] S. Ye, X. Wu, L. Wei, D. Tang, P. Sun, M. Bartlam, Z. Rao, *J. Biol. Chem.* **2007**, *282*, 2291 – 3402.
[7] P. L. Roach, I. J. Clifton, C. M. H. Hensgens, N. Shibata, C. J. Schofield, J. Hajdu, J. E. Baldwin, *Nature* **1997**, *387*, 827 – 830.
[8] E. Tamanaha, B. Zhang, Y. Guo, W. Chang, E. W. Barr, G. Xing, J. St. Clair, S. Ye, F. Neese, J. M. Bollinger, C. Krebs, *J. Am. Chem. Soc.* **2016**, *138*, 8862 – 8874.
[9] S. C. Peck, W. A. van der Donk, *J. Biol. Inorg. Chem.* **2017**, *22*, 381 – 394.
[10] E. J. Blaesi, J. D. Gardner, B. G. Fox, T. C. Brunold, *Biochemistry* **2013**, *52*, 6040 – 6051.
[11] **Tp** [tris(pyrazolyl)borate)], **TPA** [tris(2-pyridylmethyl)amine], **14-TMC** [1,4,8,11-tetramethyl-1,4,8,11-tetraazacyclotetradecane], **PyTACN** [1-(2-pyridylmethyl)-4,7-trimethyl-1,4,7-triazacyclononane], **$\mathbf{PyNMe_3}$** [4,7,10-trimethyl-1,4,7-tetraaza-2,6-pyridinophane], **BPBP** (also known as PDP) [*N,N′*-bis(2-pyridyl)-2,2′-bispyrrolidine], **N4Py** [*N,N*-bis(2-pyridylmethyl)-*N*-bis(2-pyridyl)methylamine].
[12] **L1** [3-(di(pyridin-2-yl)methyl)-1,5,7-trimethyl-2,4-dioxo-3-azabicyclo-[3.3.1]nonane-7-carboxylate], **$\mathbf{bpa^{tBu2,Me2}}$** [2-(3,5-di-*tert*-butyl-1*H*-pyrazol-1-yl)-2-(3,5-dimethyl-1*H*-pyrazol-1-yl)acetate], **bdtbpza** [2,2-bis(3,5-di-*tert*-butyl-1*H*-pyrazol-1-yl)acetate], **$\mathbf{BE^{iPr}IP}$** [3,3-bis(1-ethyl-4-iso-propyl-1*H*-imidazol-2-yl)propanoate], **$\mathbf{BM^{Me}BIP^{nPr}}$** [propyl 3,3-bis(1,4-dimethyl-1*H*-benzo[*d*]imidazol-2-yl)propanoate], **ImNNO** [2-(methoxy-bis(1-methyl-1*H*-imidazol-2-yl)methyl)phenolate], **BenzImNNO** [2-(methoxy-bis(1-methyl-1*H*-benzo[*d*]imidazol-2-yl)methyl)phenolate], **L2** [2-(bis(3,5-dimethyl-1*H*-pyrazol-1-yl)methyl)-6-(*tert*-butyl)-4-methylphenolate], **L3** [2-(bis(3,5-dimethyl-1*H*-pyrazol-1-yl)methyl)-4,6-di-*tert*-butylphenolate].
[13] H. Park, D. Lee, *Chem. Eur. J.* **2020**, *26*, 5916 – 5926.
[14] D. Sheet, T. K. Paine, *Chem. Sci.* **2016**, *7*, 5322 – 5331.
[15] J.-U. Rohde, A. Stubna, E. L. Bominaar, E. Münck, W. Nam, L. Que, Jr., *Inorg. Chem.* **2006**, *45*, 6435 – 6445.
[16] J.-U. Rohde, J.-H. In, M. H. Lim, W. W. Brennessel, M. R. Bukowski, A. Stubna, E. Münck, W. Nam, L. Que, Jr., *Science* **2003**, *299*, 1037 – 1039.
[17] E. Andris, J. Jašík, L. Gómez, M. Costas, J. Roithová, *Angew. Chem. Int. Ed.* **2016**, *55*, 3637 – 3641; *Angew. Chem.* **2016**, *128*, 3701 – 3705.
[18] V. Dantignana, J. Serrano-Plana, A. Draksharapu, C. Magallón, S. Banerjee, R. Fan, I. Gamba, Y. Guo, L. Que, Jr., M. Costas, A. Company, *J. Am. Chem. Soc.* **2019**, *141*, 15078 – 15091.
[19] J. Chen, M. Lutz, M. Milan, M. Costas, M. Otte, R. J. M. Klein Gebbink, *Adv. Synth. Catal.* **2017**, *359*, 2590 – 2595.
[20] R. Singh, G. Ganguly, S. O. Malinkin, S. Demeshko, F. Meyer, E. Nordlander, T. K. Paine, *Inorg. Chem.* **2019**, *58*, 1862 – 1876.
[21] A. R. McDonald, L. Que, Jr., *Coord. Chem. Rev.* **2013**, *257*, 414 – 428.

[22] C. Krebs, D. Galonić Fujimori, C. T. Walsh, J. M. Bollinger, *Acc. Chem. Res.* **2007**, *40*, 484 – 492.
[23] E. C. Monkcom, P. Ghosh, E. Folkertsma, H. A. Negenman, M. Lutz, R. J. M. Klein Gebbink, *Chimia* **2020**, *74*, 450 – 466.
[24] P. C. A. Bruijnincx, M. Lutz, A. L. Spek, E. E. van Faassen, B. M. Weckhuysen, G. van Koten, R. J. M. Klein Gebbink, *Eur. J. Inorg. Chem.* **2005**, 779 – 787.
[25] P. C. A. Bruijnincx, M. Lutz, A. L. Spek, W. R. Hagen, G. van Koten, R. J. M. Klein Gebbink, *Inorg. Chem.* **2007**, *46*, 8391 – 8402.
[26] A. Beck, B. Weibert, N. Burzlaff, *Eur. J. Inorg. Chem.* **2001**, 521 – 527.
[27] P. C. A. Bruijnincx, M. Lutz, J. P. den Breejen, A. L. Spek, G. van Koten, R. J. M. Klein Gebbink, *J. Biol. Inorg. Chem.* **2007**, *12*, 1181 – 1196.
[28] T. C. Higgs, C. J. Carrano, *Inorg. Chem.* **1997**, *36*, 298 – 306.
[29] M. Strianese, S. Milione, V. Bertolasi, C. Pellecchia, A. Grassi, *Inorg. Chem.* **2011**, *50*, 900 – 910.
[30] A. Beck, A. Barth, E. Hübner, N. Burzlaff, *Inorg. Chem.* **2003**, *42*, 7182 – 7188.
[31] E. Folkertsma, E. F. de Waard, G. Korpershoek, A. J. van Schaik, N. Sologabal Mirón, M. Borrmann, S. Nijsse, M. A. H. Moelands, M. Lutz, M. Otte, M.-E. Moret, R. J. M. Klein Gebbink, *Eur. J. Inorg. Chem.* **2016**, 1319 – 1332.
[32] P. D. Oldenburg, C.-Y. Ke, A. A. Tipton, A. A. Shteinman, L. Que, Jr., *Angew. Chem. Int. Ed.* **2006**, *45*, 7975 – 7978; *Angew. Chem.* **2006**, *118*, 8143 – 8146.
[33] P. C. A. Bruijnincx, M. Lutz, A. L. Spek, W. R. Hagen, B. M. Weckhuysen, G. Van Koten, R. J. M. Klein Gebbink, *J. Am. Chem. Soc.* **2007**, *129*, 2275 – 2286.
[34] I. Hegelmann, A. Beck, C. Eichhorn, B. Weibert, N. Burzlaff, *Eur. J. Inorg. Chem.* **2003**, 339 – 347.
[35] B. S. Hammes, C. J. Carrano, *Inorg. Chem.* **1999**, *38*, 3562 – 3568.
[36] A. D. Schofield, M. L. Barros, M. G. Cushion, A. D. Schwarz, P. Mountford, *Dalton Trans.* **2009**, 85 – 96.
[37] D. L. Jameson, S. E. Hilgen, C. E. Hummel, S. L. Pichla, *Tetrahedron Lett.* **1989**, *30*, 1609 – 1612.
[38] C. A. Jiménez, J. B. Belmar, *Synth. Commun.* **2007**, *37*, 2391 – 2397.
[39] Analogous triflate complexes, $\mathbf{1}^{\mathbf{OTf}}$ and $\mathbf{2}^{\mathbf{OTf}}$, could be synthesized using this procedure, substituting the MCl_2 salt for the corresponding anhydrous $M(OTf)_2$ salt. However, their isolation was hampered by the presence of unknown impurities as well as their lower stability in solution over time. Therefore, we did not pursue any subsequent coordination chemistry using these complexes. NMR data for $\mathbf{1}^{\mathrm{OTf}}$ and $\mathbf{2}^{\mathrm{OTf}}$ are given in the supporting information (Figures S59–S63).
[40] L. Falivene, Z. Cao, A. Petta, L. Serra, A. Poater, R. Oliva, V. Scarano, L. Cavallo, *Nat. Chem.* **2019**, *11*, 872 – 879.
[41] M. A. H. Moelands, S. Nijsse, E. Folkertsma, B. De Bruin, M. Lutz, A. L. Spek, R. J. M. Klein Gebbink, *Inorg. Chem.* **2013**, *52*, 7394 – 7410.
[42] K. Valegård, A. C. T. van Scheltinga, M. D. Lloyd, T. Hara, S. Ramaswamy, A. Perrakis, A. Thompson, H.-J. Lee, J. E. Baldwin, C. J. Schofield, J. Hajdu, I. Andersson, *Nature* **1998**, *394*, 805 – 809.
[43] Y. Uragami, T. Senda, K. Sugimoto, N. Sato, V. Nagarajan, E. Masai, M. Fukuda, Y. Mitsui, *J. Inorg. Biochem.* **2001**, *83*, 269 – 279.
[44] W. L. Steffen, G. J. Palenik, *Acta Crystallogr. Sect. B* **1976**, *32*, 298 – 300.
[45] D. F. Evans, *J. Chem. Soc.* **1959**, 2003 – 2005.
[46] G. J. Long, P. J. Clarke, *Inorg. Chem.* **1978**, *17*, 1394 – 1401.
[47] T. M. U. Ton, C. Tejo, S. Tania, J. W. W. Chang, P. W. H. Chan, *J. Org. Chem.* **2011**, *76*, 4894 – 4904.
[48] J. N. Smith, Z. Shirin, C. J. Carrano, *J. Am. Chem. Soc.* **2003**, *125*, 868 – 869.
[49] S.-J. Chiou, C. G. Riordan, A. L. Rheingold, *Proc. Natl. Acad. Sci. USA* **2003**, *100*, 3695 – 3700.
[50] J. Notni, H. Görls, E. Anders, *Eur. J. Inorg. Chem.* **2006**, 1444 – 1455.
[51] S.-J. Chiou, J. Innocent, C. G. Riordan, K.-C. Lam, L. Liable-Sands, A. L. Rheingold, *Inorg. Chem.* **2000**, *39*, 4347 – 4353.
[52] U. Brand, M. Rombach, J. Seebacher, V. Heinrich, *Inorg. Chem.* **2001**, *40*, 6151 – 6157.
[53] M. M. Ibrahim, J. Seebacher, G. Steinfeld, H. Vahrenkamp, *Inorg. Chem.* **2005**, *44*, 8531 – 8538.
[54] J. J. Wilker, S. J. Lippard, *J. Am. Chem. Soc.* **1995**, *117*, 8682 – 8683.
[55] X.-W. Song, C. Guo, C.-N. Chen, *Z. Anorg. Allg. Chem.* **2017**, *643*, 2110 – 2115.
[56] R. K. Dean, C. I. Fowler, K. Hasan, K. Kerman, P. Kwong, S. Trudel, D. B. Leznoff, H.-B. Kraatz, L. N. Dawe, C. M. Kozak, *Dalton Trans.* **2012**, *41*, 4806.
[57] T. A. Enache, A. M. Oliveira-Brett, *J. Electroanal. Chem.* **2011**, *655*, 9 – 16.
[58] Y. S. Tan, S. Chen, W. M. Hong, J. M. Kan, E. S. H. Kwek, S. Y. Lim, Z. H. Lim, M. E. Tessensohn, Y. Zhang, R. D. Webster, *Phys. Chem. Chem. Phys.* **2011**, *13*, 12745.
[59] N. L. Zabik, C. N. Virca, T. M. McCormick, S. Martic-Milne, *J. Phys. Chem. B* **2016**, *120*, 8914 – 8924.
[60] S. Itoh, M. Taki, H. Kumei, S. Takayama, S. Nagatomo, T. Kitagawa, N. Sakurada, R. Arakawa, S. Fukuzumi, *Inorg. Chem.* **2000**, *39*, 3708 – 3711.
[61] J. A. Halfen, B. A. Jazdzewski, S. Mahapatra, L. M. Berreau, E. C. Wilkinson, L. Que, Jr., W. B. Tolman, *J. Am. Chem. Soc.* **1997**, *119*, 8217 – 8227.
[62] V. W.-W. Yam, Y.-L. Pui, K.-K. Cheung, N. Zhu, *New J. Chem.* **2002**, *26*, 536 – 542.
[63] B. Adam, E. Bill, E. Bothe, B. Goerdt, G. Haselhorst, K. Hildenbrand, A. Sokolowski, S. Steenken, T. Weyhermüller, K. Wieghardt, *Chem. Eur. J.* **1997**, *3*, 308 – 319.
[64] J. B. Gordon, A. C. Vilbert, I. M. DiMucci, S. N. MacMillan, K. M. Lancaster, P. Moënne-Loccoz, D. P. Goldberg, *J. Am. Chem. Soc.* **2019**, *141*, 17533 – 17547.
[65] D. Wang, K. Ray, M. J. Collins, E. R. Farquhar, J. R. Frisch, L. Gómez, T. A. Jackson, M. Kerscher, A. Waleska, P. Comba, M. Costas, L. Que, Jr., *Chem. Sci.* **2013**, *4*, 282 – 291.
[66] T. Yu, V. K.-M. Au, D. P.-K. Tsang, M.-Y. Chan, V. W.-W. Yam, *Dalton Trans.* **2015**, *44*, 18983 – 18992.
[67] T. Lu, F. Chen, *J. Comput. Chem.* **2012**, *33*, 580 – 592.

Manuscript received: October 20, 2020
Accepted manuscript online: December 16, 2020
Version of record online: February 24, 2021

